MATERIALS SCIENCE

Interfacial superstructures and chemical bonding transitions at metal-ceramic interfaces

Can Yang[1]*, Chongze Hu[2]*, Congying Xiang[1], Hongbo Nie[3], Xinfu Gu[4], Lin Xie[5], Jiaqing He[5], Wenqing Zhang[5], Zhiyang Yu[1,5,6†], Jian Luo[2†]

Metal-ceramic interfaces are scientifically interesting and technologically important. However, the transition of chemical bonding character from a metal to a nonoxide ceramic is not well understood. The effects of solute segregation and interfacial structural transitions are even more elusive. In this study, aberration-corrected electron microscopy is combined with atomic-resolution energy-dispersive x-ray and electron energy loss spectroscopy to investigate Ti-, V-, and Cr-segregated WC-Co interfaces as model systems. The experiments reveal the general anisotropic formation of reconstructed trilayer-like superstructures with segregant-specific compositional profiles that facilitate the transition from covalent to metallic electronic structures. Density functional theory calculations confirm the gradual increasing metallicity from WC to Co in the interfacial trilayers via increasing metallic solute concentration. This study uncovers unprecedented details of the sophisticated interfacial superstructures at metal-ceramic interfaces. It sheds light on into how a metal transits to a ceramic at a "general" interface with strong segregation.

INTRODUCTION

Metal-ceramic interfaces are of great technological importance, e.g., in cermets, catalysts, electronic and electrochemical devices, and engines components (1, 2). Of particular scientific interests are to understand the transitions of bonding characters at metal-ceramic interfaces, with dissimilar electronic structures at the two sides, and how they are coupled with the interfacial structural and compositional variations. Prior studies largely focused on the "clean" (undoped and coherent) metal-oxide interfaces, where the charge transfers at the interface give rise to relatively simple transitions from ionic to metallic bonding (3). For instance, electrons were found to transfer from Nb to the outmost O layers of the Al_2O_3 (0001) plane to form ionic Nb—O bonds (4). Incoherent phase boundaries are substantially more complex and much less understood. For example, prior density functional theory (DFT) calculations of the interface between Ni (111) and Y_2O_3-stabilized ZrO_2 (111) suggested that the incoherency may result in the coexistence of metal cations and metal-oxygen bonding pairs to produce site-dependent bonding characters (5).

Solute segregation (also known as adsorption) can further induce interfacial structural transitions and alter bonding characters, thereby influencing the interfacial adhesion (6), electronic (7), and other properties of the metal-ceramic interfaces. Moreover, segregation can induce the formation and transition of two-dimensional (2D) interfacial phases, which were named as "complexions" to differentiate them from thin layers of 3D bulk phases precipitated at the interfaces (8–12). Via advanced aberration-corrected electron

microscopy (13–15) and modeling (16, 17), a spectrum of distinct driving forces of segregation, e.g., strain relaxation (18, 19), compensation of space charges (20–22), and adaption of coordination environments (17), have been revealed for the metallic and ceramic grain boundaries. Yet, the segregation at the metal-ceramic interfaces, particularly its interplay with the transition of the chemical bonding character, is not well understood.

The naturally formed transition metal–segregated WC-Co phase boundaries are good model systems to investigate the metal-ceramic interfaces. In WC, W—C bonds are largely covalent with partial ionic characters, and W—W bonds are metallic; the bonding in the cobalt side is purely metallic. How the chemical bonding character transits at the WC-Co interface has not been examined by high-resolution methods. Moreover, transition metal dopants, such as Ti, V, and Cr, can segregate at the WC-Co interfaces to induce cubic-like interfacial reconstructions (23–29), which can presumably influence the interfacial transition of chemical bonding characters. Thus, direct measurements of both compositional and electronic structures at the atomic resolution are critically needed but have not been reported previously.

In this study, we combine a variety of aberration-corrected scanning transmission electron microscopy (AC-STEM) techniques, including high-angle annular dark-field (HAADF; for metal atoms) and integrated differential phase contrast (iDPC; for resolving lightweight carbon atoms), along with atomic-resolution energy-dispersive x-ray spectroscopy (EDS) and electron energy loss spectroscopy (EELS), with DFT calculations to investigate the Ti-, V-, and Cr-segregated WC-Co interfaces as the model systems. The atomic configuration, compositional profiles, and electronic structures are all measured at atomic resolutions simultaneously to uncover unprecedented details. This study aims to answer an open scientific question: How does a metal transit to a mostly covalent ceramic at a "general" interface with strong segregation?

RESULTS

Interfacial reconstruction

WC grains exhibit prominent faceting with the addition of grain growth inhibitor, including Ti (Fig. 1A), V, and Cr (fig. S1). The

[1]State Key Laboratory of Photocatalysis on Energy and Environment, College of Chemistry, Fuzhou University, Fuzhou, Fujian 350002, P. R. China. [2]Department of NanoEngineering, Program of Materials Science and Engineering, University of California San Diego, La Jolla, CA 92093, USA. [3]School of Materials Science and Engineering, Baise University, Baise 533000, P. R. China. [4]School of Materials Science and Engineering, University of Science and Technology Beijing, Beijing 100083, P. R. China. [5]Department of Physics, Southern University of Science and Technology, Shenzhen, Guangdong 518055, P. R. China. [6]Xiamen Tungsten Co. Ltd., Xiamen, Fujian 361126, P. R. China.
*These authors contributed equally to this work.
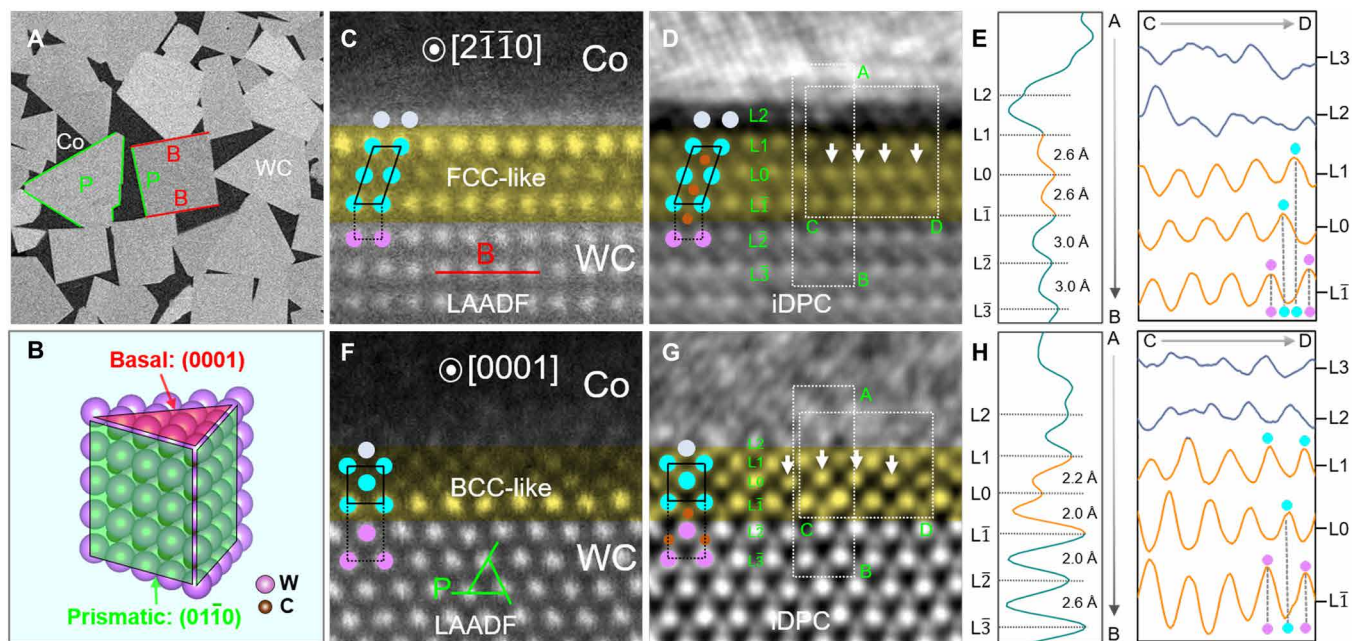†Corresponding author. Email: jluo@alum.mit.edu (J.L.); yuzyemlab@fzu.edu.cn (Z.Y.)

Fig. 1. The formation of reconstructed FCC- versus BCC-like interfacial trilayers at the Ti-segregated WC-Co interfaces on the B and P planes of WC. (**A**) SEM image of a WC-Co composite, where characteristic B and P planes of WC grains are denoted by red and green lines, respectively. (**B**) Schematic of the WC grain morphology. Pairs of atomic-resolution AC LAADF and iDPC images and line profile analysis (integrated vertically along A➔B direction or horizontally along C➔D direction for each layer) of WC-Co interfaces on B (**C** to **E**) and P (**F** to **H**) facets, respectively. The yellow color is used to highlight the (FCC- or BCC-like) reconstructed interfacial trilayers. The central layer of the reconstructed interfacial trilayers is defined as the L0 layer. The layers at the WC side are labeled as L$\bar{1}$, L$\bar{2}$, etc., while those at the Co side are denoted as L1, L2, etc.

interfaces in WC-Co composites contain naturally formed WC-Co phase boundaries and WC grain boundaries. Both are evidently faceted (Fig. 1A). The WC grains typically have truncated triangular and rectangular cross sections near the [0001] and [2$\bar{1}\bar{1}$0] directions, respectively. As a result, the equilibrium grain morphology of WC grains could be represented by a prism enclosed by two basal (B; {0001}) planes and three prismatic (P; {10$\bar{1}$0}) facets (Fig. 1B). Electron backscatter diffraction (EBSD) analysis reveals wide-spreading existence of WC(B)-Co and WC(P)-Co interfaces in the Ti-, V-, and Cr-doped samples, accounting for 65, 61, and 70%, respectively, of the overall interfaces (fig. S2).

Thin lamellae containing WC-Co interfaces were extracted by focused ion beam (FIB) for TEM. An advanced TEM characterization technique, iDPC, was applied to reveal the atomic structures, particularly the light carbon atoms at the atomic resolution. The iDPC signal corresponds to the integrated phase shift in the beam direction so that bright spots can be simply interpreted as atomic columns (*30*), rendering it a better alternative of annular dark-field (ADF) to resolve lightweight atoms. A pair of concurrently recorded low-angle annular dark-field (LAADF) and iDPC images is presented in Fig. 1 (C and D), with the trilayer-like reconstructed interfacial regions highlighted by yellow color. The LAADF image only resolves the metal skeleton, while the iDPC image indicates that carbon atoms occupy the interstitial sites. Line profile analysis of the iDPC image (Fig. 1E) reveals a reconstructed interfacial trilayer with FCC (face-centered cubic) stacking sequences on the B plane, where the metal skeletons are octahedrally surrounded by interstitial carbon atoms. This proposed structure is further confirmed from another projection along [10$\bar{1}$0] (fig. S3).

A similar interfacial reconstruction is identified at the WC(P)-Co interfaces. As shown in the LAADF image (Fig. 1F), atomic ordering also occurs in a trilayer superstructure (the L$\bar{1}$ to L1 layers). Partially ordered L2 or even L3 layers on the Co side could be discerned with low contrast. Carbon atoms are clearly resolved in the WC lattice, while they are absent in the interstitial sites of the superstructures (Fig. 1G). Thus, the WC(P)-Co interface exhibits a reconstructed interfacial trilayer with BCC (body-centered cubic) stacking sequence (Fig. 1H), which is further confirmed from the [2$\bar{1}\bar{1}$0] projection (fig. S4). Such BCC-like interfacial trilayers consisting of a pure metallic framework have not been reported before (*25*, *28*, *31*).

The extent of partial ordering into the Co side depends on the orientation relationship between the WC and Co phases. When the coherency is low, TEM could only resolve ordered trilayer structures, e.g., in a WC(B)-Co (fig. S5) interface. In other instances, the lattice fringe could extend several (>5) layers into the Co phase at semicoherent WC(B)-Co and WC(P)-Co interfaces (fig. S6). We also note that the atomic configuration of the L2 layer (if visible) is different from those in the FCC-like interfacial trilayers. For instance, the characteristic interstitial carbon atoms in the FCC-like interfacial trilayers are missing between the L1 and L2 layers (Fig. 1D). Hence, the ordered trilayers on the WC side are likely intrinsic segregation patterns at the interfaces, while the imposed ordering decays away in the Co sides (in L2, L3, etc.). This complexity, which might lead to different conclusions (or misinterpretations) with lower-resolution imaging techniques, can help explain the large discrepancies in the variation of the thicknesses of the WC-Co interfacial complexions in literatures (*25*, *31*).

Compositional profiles

Atomic-resolution EDS mapping was used to investigate the compositional profiles across the WC-Co interfaces. For parallel comparison, the EDS signals of each layer were integrated from the corresponding EDS maps, followed with composition quantification that provided spatial distribution of the constitutional solutes across the interfaces. Limited by the low x-ray yield and undesired contamination of carbon elements, we did not include it in the EDS quantification to reduce errors. However, it could be unequivocally concluded from iDPC imaging that the WC(B)-Co complexion contains a high amount of carbon, while the WC(P)-Co is carbon deficient (as discussed above).

Several interesting observations can be found in Fig. 2. First, the atomic structures of the Ti-, V-, and Cr-doped WC-Co interfaces are similar, as shown by the HAADF images. Similar reconstructed interfacial trilayers persist in the specimens examined, irrespective of transition metal dopants. However, the interfacial reconstructions depend on the orientation of terminating WC grain surface, forming FCC-like trilayers on B (Fig. 2, A and B) facets versus BCC-like trilayers on P (Fig. 2, E and F) facets of WC grains, respectively. Second, the segregation profiles depend on both the (B or P) facet and the (V, Ti, or Cr) dopant. On the B facets of WC, Ti atoms mainly segregate to the L0 layer, while the segregation of V and Cr spread from the L$\bar{1}$ to L1 layers (Fig. 2C). On the P facets of WC, the Ti segregation level is below the EDS detection limit (Fig. 2G). A minor amount of V and a high fraction of Cr solutes are accommodated in the BCC-like interfacial trilayer (from the L$\bar{1}$ to L1 layers; Fig. 2G). Third, the reconstructed interfacial trilayers consist of mixed cations of Co, W, and solute atoms (table S1) with compositional gradients. Mixing of elements and composition gradients are found in the highly ordered interfacial superstructures, in contrast to the previous prevailing understandings of the WC-Co interfaces (31–34).

DFT calculations of interfacial reconstruction

On the basis of the chemical compositions measured by EDS, we constructed DFT simulation cells by considering reconstruction of
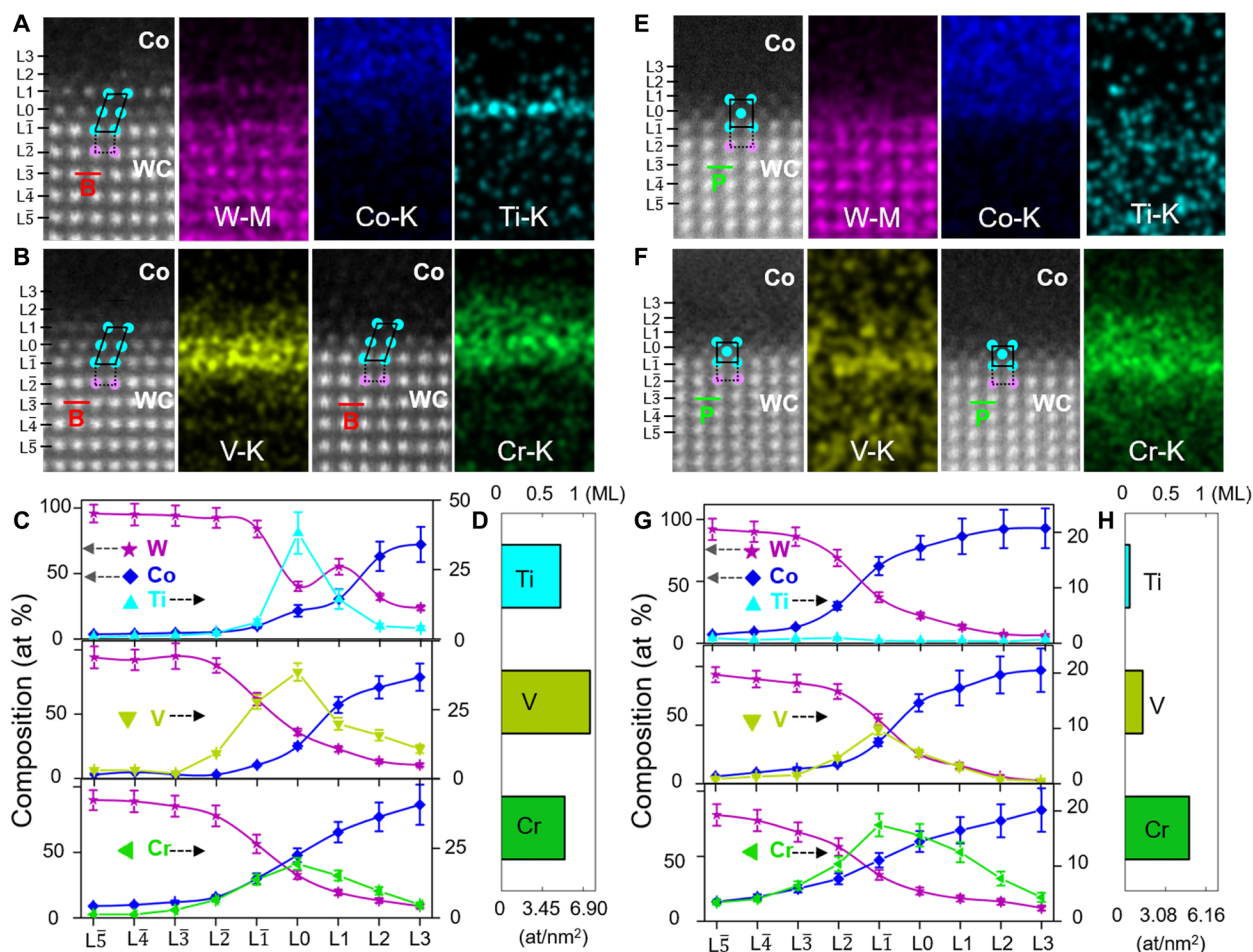

Fig. 2. Atomic-resolution compositional profiles of the Ti-, V-, and Cr-doped WC-Co interfaces measured by quantitative EDS. (**A**) Enlarged HADDF image of a Ti-doped WC(B)-Co interface and EDS maps of W, Co, and Ti. (**B**) Enlarged HADDF image of the V- and Cr-doped WC(B)-Co interfaces and EDS maps of V and Cr. The EDS maps for all elements for the V- and Cr-doped cases are given in fig. S7. (**C**) Measured compositional profiles of the three interfaces. atomic %, at %. (**D**) Overall segregation amount of the three dopants at the WC(B)-Co interface. (**E**) Enlarged HADDF image of a Ti-doped WC(P)-Co interface and EDS maps of W, Co, and Ti. (**F**) Enlarged HADDF image of the V- and Cr-doped WC(P)-Co interfaces and EDS maps of V and Cr. The EDS maps for all elements for V- and Cr-doped cases are shown in fig. S8. (**G**) Measured compositional profiles of the three interfaces. (**H**) Overall segregation amounts (GB excesses) of the three dopants at the WC(P)-Co interface. The interfacial excesses of solutes shown in (D) and (H) are integrated from the L$\bar{5}$ to L3 layers.

both the B- and P-faceted interfaces. The DFT-optimized interfacial structures are in good agreement with experiments (Fig. 3, A and B, versus fig. S9). For example, DFT-optimized Ti-doped WC(B)-Co interface exhibits highly ordered density profile from the L$\bar{1}$ to L1 layers, while the L2 layer (in the Co side) shows some structural disorder, consistent with the measured intensity profiles by iDPC (Fig. 1).

To understand the interfacial reconstruction, we calculate the energy difference: $\Delta E_{Diff} = E_{non-FCC(BCC)} - E_{FCC(BCC)}$, where $E_{non-FCC(BCC)}$ and $E_{FCC(BCC)}$ are the total energies of the interfaces without and with the reconstruction, respectively. Figure 3C shows that B-faceted interface without the FCC reconstruction is always stable (with positive ΔE) when there is no segregation. By increasing the doping concentrating of Ti, V, and Cr, ΔE becomes negative, stabilizing FCC-like interfacial trilayers. In other words, FCC-like reconstruction at the B-faceted interface is induced by segregation. However, for the P-faceted interface, ΔE_{Diff} is always small (on the order of a few millielectron volts/atom) and is independent of doping concentration. Thus, DFT calculations do not have sufficient accuracies to predict the stable structure.

Next, we calculate the segregation energy for each dopant element. Figure 3D shows the calculated segregation energy ΔE_{Seg} by moving the dopant from the Co side to the interface (the L$\bar{1}$ to L1 layers) in the B-faceted interface. First, the ΔE_{Seg} of all solute atoms in the FCC-like interfacial trilayer is always smaller than that in the unreconstructed (non-FCC) interface, indicating preferential segregation in the FCC-like interfacial trilayers. Second, the calculated ΔE_{Seg} of Ti always has the lowest energy at the L0 layer, indicating favorite segregation of Ti. This is in good agreement with the EDS measurement that Ti has the largest concentration in the L0 layer. Third, for the elemental segre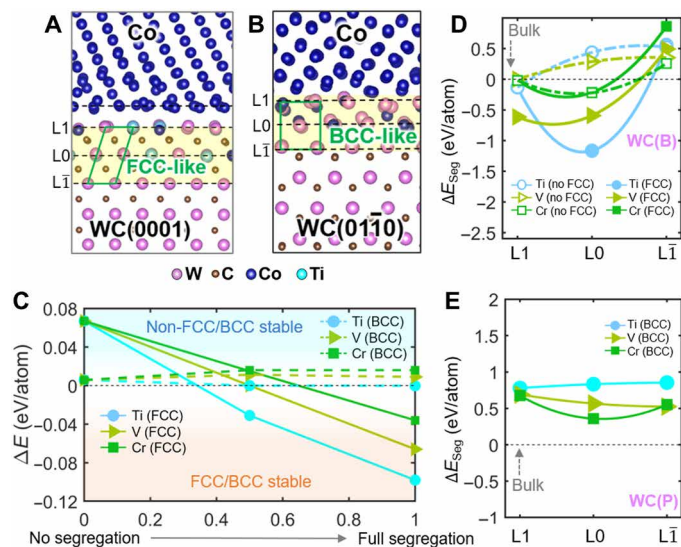gation at the P-faceted interface, the positive ΔE_{Seg} indicates unfavorable segregation of all elements from the Co side to the interface (Fig. 3E). By calculating the ΔE_{Seg} from the WC side, the negative ΔE_{Seg} suggests that the segregation at the P-faceted interface is likely to occur (fig. S10). Meanwhile, the lowest ΔE_{Seg} of the Cr atom indicates that Cr is favorable to segregate at the P-faceted plane, which is consistent with high propensity of Cr segregation measured from EDS experiments. Last, by comparing the ΔE_{Seg} between the B-faceted and P-faceted interfaces, both Ti and V have much smaller ΔE_{Seg} in the WC(B)-Co interfaces, which explains the preferential segregation of Ti and V on WC B planes. On the other hand, for Cr, both B and P facets have comparable ΔE_{Seg}, thereby indicating similar segregation tendency.

Electronic structure transitions revealed by EELS

Atomic-resolution EELS spectra were acquired on each atomic layer to elucidate the transition in the electronic structure at the WC-Co interfaces. Here, Co, V, Cr, and Ti all belong to $3d$ transitional elements that could generate evident $L_{2,3}$ white lines. They consist of two independent L_2 and L_3 peaks that resulted from transitions from the occupied $2p$ ($2p_{1/2}$ and $2p_{3/2}$) states to the unoccupied $3d$ states. For Cr and Co solute atoms with more than four $3d$ electrons, a higher occupancy of $3d$-orbital would reduce the L_3 transition probability (35, 36), causing a decrease in the white line ratio (L_3/L_2). Thus, a quantitative analysis of L_3/L_2 ratios could qualitatively depict the charge transfer and bond environment transition across the interface.

We acquired Co EELS spectra from the WC(B)-Co and the WC(P)-Co interfaces, as well as the Co phase, of a Cr-doped sample. For an easy comparison, all the spectra were normalized by setting the pre-edge background to 0 and the L_3 peak to 255, respectively (Fig. 4A). The Co signals at the L$\bar{1}$ and L0 layers are slightly noisy because of low solute concentrations. Nonetheless, a decrease in the intensities of the Co L_2 peaks from WC to Co could be recognized on both the B and P facets (Fig. 4A). The L_3/L_2 ratios increase monotonically from the L$\bar{1}$ to L1 layer within both WC(B)-Co and WC(P)-Co complexions (Fig. 4B), thereby suggesting a transition of bonding environments from more covalent (higher occupancy of the $3d$ band) in the L$\bar{1}$ layers to more metallic in the L1 layer. Similar trends in the electronic structure transitions were confirmed for Ti- (fig. S11) and V-doped (fig. S12) WC(B)-Co and WC(P)-Co interfaces as measured from Co $L_{2,3}$ peaks. Thus, transitions in the bonding environments in the reconstructed interfacial trilayers are universal.

The bonding environments of Cr, V, and Ti solutes were also carefully examined. In the Cr-doped sample, the L_3 peak of Cr is lower than the L_2 peak in the L$\bar{1}$ layer, while the trend is reversed in the L1 layer (Fig. 4C). The profiles of L_3/L_2 ratios were identified across both Cr-doped WC(B)-Co and WC(P)-Co interfaces (Fig. 4D), which reveal changes in the electronic structures. However, the situations are different in the Ti- and V-doped samples. The EELS signal and L_3/L_2 ratio of V (fig. S13) and Ti (fig. S14) do not change within the WC(B)-Co superstructures, which is indicative of unchanged bonding environments near those solute atoms.

DFT calculations of the electronic structure transitions

We calculated the electron localization function (ELF) to further understand the transition of the electronic structure at the WC-Co interfaces. Using the optimized structures with Ti doping, the Co ELF maps (Fig. 5A) show that electrons are strongly localized between
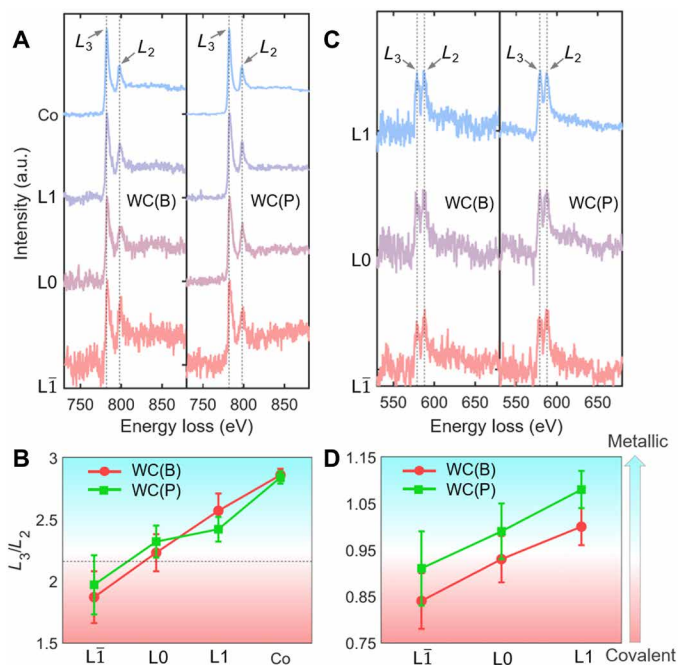

Fig. 3. DFT calculations of the WC-Co interfaces. (**A** and **B**) DFT-optimized Ti-doped WC(B)-Co and WC(P)-Co interfacial structures based on the elemental compositional profiles measured by EDS. (**C**) The energy difference between the interfacial structures before and after the reconstructions as a function of segregation concentration at the L$\bar{1}$ and L0 layers. (**D**) Calculated segregation energy ΔE_{Seg} by moving solute atoms from Co to different layers in the WC(B)-Co interface. (**E**) Calculated segregation energy ΔE_{Seg} by moving solute atoms from Co to different layers in the WC(P)-Co interface.

Fig. 4. Electronic structure transitions at the WC-Co interfaces by atomic-resolution EELS. (**A**) Normalized Co $L_{2,3}$ EELS spectra recorded across the WC(B)-Co and WC(P)-Co interfaces of Cr-doped samples. a.u., arbitrary unit. (**B**) L_3/L_2 ratios of the EELS spectra in (A). (**C**) Normalized Cr $L_{2,3}$ EELS spectra recorded across the WC(B)-Co and WC(P)-Co interfaces of Cr-doped samples. (**D**) The corresponding L_3/L_2 ratio reveals electronic structure transitions of Cr solutes. In (B) and (D), red color refers to bonding environment with more covalent component, and green color represents more metallic characters.

Co and C atoms at the L$\bar{1}$ and L0 layers of the B-faceted interface, indicating strong covalent interactions. At the L1 layer, the ELF maps show that electrons are distributed between these atoms in a homogeneous manner for the Co atoms, suggesting a metallic character (Fig. 5A). Thus, there are through-thickness gradients in the bonding environment in the WC(B)-Co trilayers over the three atomic layers, with a transition from strong covalency in the L$\bar{1}$ layer to metallicity in the L1 layer, in good agreement with the EELS measurements.

For the WC(P)-Co interface (Fig. 5B), ELF maps show that the electrons are concentrated at Co—C bonds in the L$\bar{1}$ layer with covalent character. Because the BCC-like interfacial trilayer consists of a metal lattice without interstitial carbon atoms, most Co atoms at the L0 layer form bonds with W atoms (Fig. 5B), which results in weakly localized electrons at Co—W bonds and reduced covalency. The electrons are homogeneously shared for the metal atoms at the L1 layer with clear metallic bonding character (Fig. 5B). In summary, DFT calculations revealed that the electronic structure transition also mainly occurs in the ordered interfacial trilayers on the B or P plane, consistent with the EELS analysis.

To reveal the intrinsic bonding states across the interfaces, we calculated partial density of states (PDOS) for each element. Since the major density of states (DOS) of transition metals is dominated by d bands near Fermi level (E_F) (37, 38), we only plot their d-orbitals. Figure 5 (C and D) shows the PDOS profiles of each element from the L$\bar{1}$ to L1 layers in Ti-doped B- and P-faceted interfaces. By examining the PDOS magnitude of Co at E_F, we found that the DOS of Co d-orbital increases from the L$\bar{1}$ to L1 layers for both interfaces.

Since the metal bonding character is proportional to the DOS value at E_F (38), the increase in the Co d-orbital states from the L$\bar{1}$ to L1 layers indicates the enhancement of metallic bonding. Besides, the DOS of Co atoms always have large overlaps with surrounding C atoms at the WC side but smaller overlaps at the Co side. For example, in the B-faceted interface (Fig. 5C), the PDOS of Co at the L$\bar{1}$ and L0 layers, respectively, exhibit two strong peaks at −3.5 and −5 eV (red arrows), which overlaps with large C p-orbital states from −7.5 to −2.5 eV. However, for Co atoms at the L1 layer, the peak of d-orbital states near −5 eV is missing (gray arrow in Fig. 5C), which suggests the weakening of the covalent interaction between Co and C atoms. For P-faceted interfaces (Fig. 5D), Co atoms in the L$\bar{1}$ layer exhibit some d-orbital states from −7.5 to −5 eV (indicated by the red arrow), which can be attributed to the covalent interaction with p-orbitals of the nearby C atoms. However, these Co d-orbital states almost disappear at the L0 and L1 layers (indicated by the gray arrows in Fig. 5D), thereby suggesting the inhibition of covalent interaction. Similar electronic structure transitions could be observed in the PDOS analysis of the Cr-doped WC-Co interfaces (Fig. 5, E and F), in terms of Co bonding states. Therefore, the PDOS analysis demonstrates that the reconstructed interfacial trilayers create graded bonding environments from covalency in the WC side to metallicity in the Co side, in good agreements with our EELS experiments. Such transitions are universal for the Ti-, V-, and Cr-doped interfaces.

DISCUSSION

In brief, we have discovered the gradual transitions in bonding characters across the Ti-, V-, and Cr-doped WC-Co interfaces with anisotropic segregation-induced interfacial reconstructions with general reconstruction characters but segregant-specific sophisticated compositional profiles. While prior studies discovered interfacial reconstructions via atomic-resolution imaging (24–28), this study first measured the electronic structures and compositional profiles at atomic resolution simultaneously to reveal transition of the bonding characters, which are further validated by DFT calculations. Specifically, this study has revealed that the reconstructed interfacial trilayers on both B and P facets contain mixed bonding environments; in both cases, the bonding is more covalent in the L$\bar{1}$ layers on the WC side, but it becomes more metallic in the L1 layer on the Co side. This is universal for Ti-, V-, and Cr-doped WC-Co interfaces for both facets, albeit the detailed atomic-level compositional profiles are substantially different for each of the six cases (Fig. 2).

Because of the presence of covalent components at the interface, the lattice coherence between the reconstructed interfacial trilayers and the WC lattice can be understood. On the one hand, our study using iDPC imaging has directly revealed that the interfacial trilayer on the B facet contains a high amount of interstitial carbon atoms, which indicates strong covalent and rigid bonding. This helps stabilize a highly ordered interfacial superstructure. On the other hand, the covalency is reduced and replaced by stronger metallic bonds on the P-faceted interfaces, which causes atomic structural disorder, especially in the Co side (see the arrows in Figs. 1G and 5B). It is because the metallic bonds are neither directional nor rigid, allowing distorted atomic configurations.

We found that the reconstructed interfacial trilayers universally exist in the Ti-, V-, and Cr-doped WC-Co interfaces on two WC facets with different interfacial misorientations. Recently, Li et al. (39) discovered that Si segregates at the TiB$_2$ side of the TiB$_2$-Al
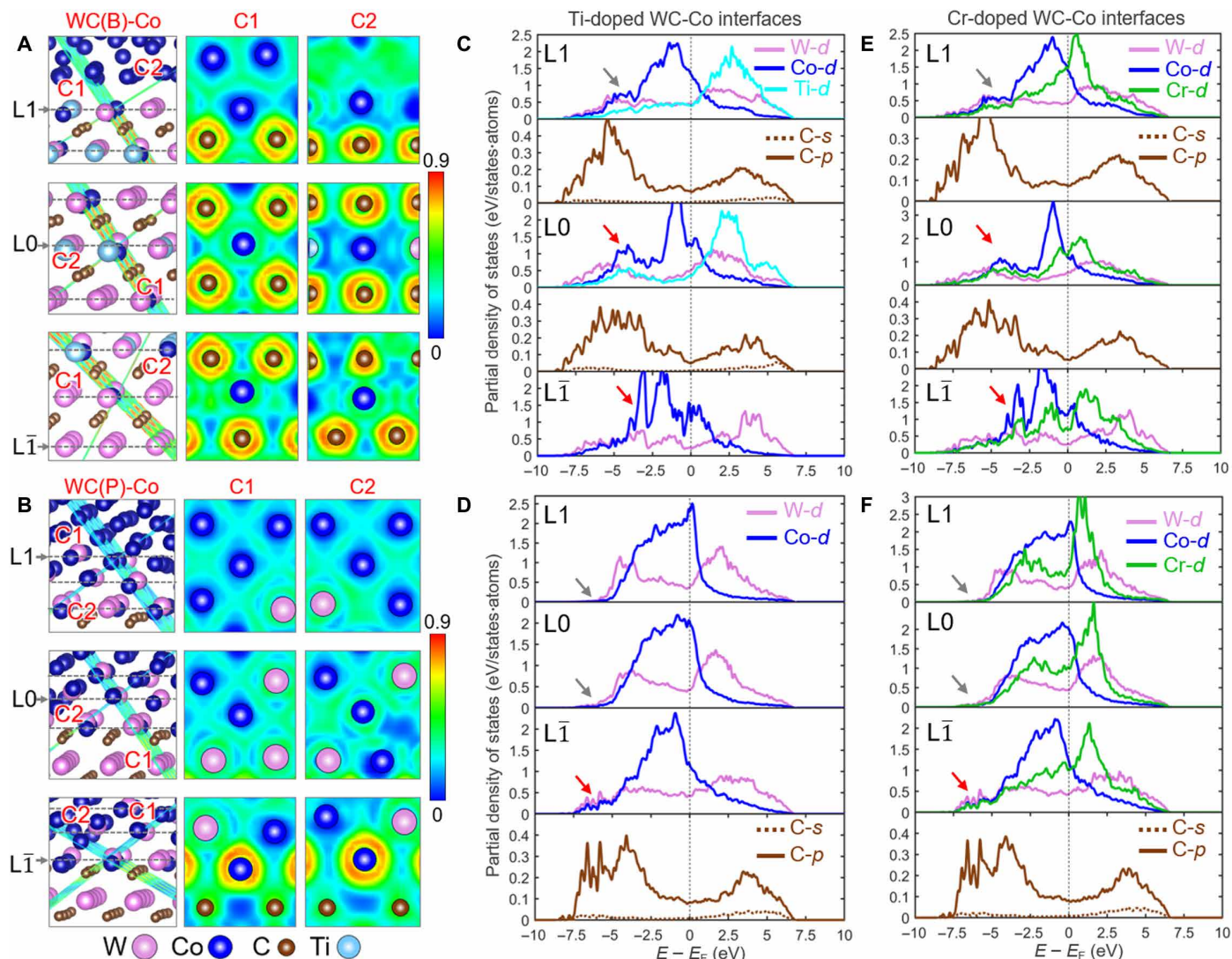
Fig. 5. Electronic structures at the WC-Co interfaces by DFT calculations. (**A** and **B**) ELF of the DFT-optimized structures of Ti-doped WC(B)-Co and WC(P)-Co interfaces based on experimental compositions. We use C1 and C2 planes to display the 3D bonding environments at different layers of the interfacial superstructure. Color bars on the right indicate the electronic densities. (**C** and **D**) PDOS evolution from the L$\bar{1}$ to L1 layer for the Ti-doped WC(B)-Co and WC(P)-Co interfaces. (**E** and **F**) PDOS evolution from the L$\bar{1}$ to L1 layer for the Cr-doped WC(B)-Co and WC(P)-Co interfaces.

interfaces with lattice coherency but compositional gradients. This suggests that at least some features discovered here may also exist in other metal-ceramic interfaces.

Furthermore, the current study provides a deeper insight into the segregation of Ti, V, and Cr at the WC-Co interfaces. We examined the coordination environments of a variety of Ti-, V-, and Cr-based carbides according to the Materials Project database (*40*). The coordination numbers of most stable carbides are ~6, 5, and 3 for TiC, V_6C_5, and Cr_7C_3, respectively. Here, Ti prefers to have coordination of six, and the cubic TiC is the most stable phase. As a result, Ti atoms segregate at the strong covalent bonded L$\bar{1}$ or L0 layers of WC(B)-Co interfaces to form TiC-like (FCC-like) interfacial trilayers. In contrast, the interfacial trilayers in the WC(P)-Co interfaces are nearly free from Ti segregation, since the carbon-depleted structure cannot offer the six-carbon-coordination environment. Moreover, the L0 layer provides a similar octahedral coordination compared

with that of TiC, while the L$\bar{1}$ layer offers a distorted octahedral coordination. It helps to explain the preferential segregation of Ti in the L0 layer (versus the L$\bar{1}$ layer) from the consideration of coordination environments (*17*).

The most stable phase of chromium carbide is nonstoichiometric Cr_7C_3, which indicates that Cr could form not only covalent bonds with carbon but also metallic bonds with the neighboring Cr atoms. Hence, Cr segregates at both the B and P facets with high amounts over several atomic distances (Fig. 2, D and H) because of its excellent adaptability to both metallic and covalent environments. The bonding characters of V_6C_5 are between those for Cr_7C_3 and TiC. Consequently, the segregation behaviors of V to WC-Co interfaces are also in between (Fig. 2, D and H).

Note that a variety of other solute atoms, including Ta and Nb, were reported to segregate the reconstructed interfacial layers (*26*). When two codopants (e.g., V and Cr) were used together in the

WC-Co composites to maximize grain growth inhibition ability, V and Cr can cosegregate at the WC-Co interfaces (*41*). The current findings should be extendable to other transition metal–doped WC-Co systems.

Notably, the detailed interfacial structures revealed here can further help to understand the underlying grain growth inhibition mechanisms via more realistic DFT modeling. Without the measured atomic-level compositional profiles, prior studies usually treated the interface as thin cubic films with evenly mixed W, C, and dopant atoms [typically denoted as $(MW)C_x$, where M is a dopant]. Only one atomic probe tomography study suggested a high Co content up to 1.2 monolayer in the interfacial layer (*42*), which is consistent with our observation. Thus, the detailed compositional and structural profiles measured in this study with unprecedented details can help establish more accurate atomic models to better understand the grain growth inhibition mechanisms.

Last, detailed atomic-level observations based on a combination of advanced microscopy imaging modes made in this study may help explain the large discrepancies in the thicknesses of WC-Co interfacial complexions reported in literatures (*26–29*, *43*, *44*). Previous research on WC-Co interfaces reported similar cubic-like complexions, but the reported thicknesses were often inconsistent. The thicknesses of the complexions in literatures on WC B planes were in the range of one to five atomic layers (*26–29*, *43*, *44*). Recently, an AC-STEM study revealed a bilayer-like complexion (consisting of a Ti-rich inner layer and a W-rich outer layer) on the WC B planes (*25*). However, another high-resolution electron microscopy (HREM) work claimed the existence of four Ti-containing atomic layers on a same B plane (*31*), which were observed in a nanocrystalline sample with high interfacial coherency between WC and Co phases. Here, we suggested that the different measured thicknesses of the interfacial layers might be a result of different levels of extended partial orders from the WC side, similar to those shown in fig. S6B, which can cause artifacts in different imaging models (particularly HREM imaging with delocalization), in addition to the ambiguity in defining the start and end points of the interfacial layers. Here, a combination of advanced imaging modes in AC-STEM, along with atomic-level compositional analysis, can resolve such sublet differences and help establish exact atomic-resolution profiles of the structure, composition, and bonding characters simultaneously to eliminate any ambiguity.

In summary, atomic-resolution HAADF and iDPC imaging, EDS mapping, and EELS analysis are combined to examine the atomic configurations, compositional profiles, and bonding characters across the Ti-, V-, and Cr-doped WC-Co interfaces. This study demonstrates that the anisotropic formation of interfacial trilayers with general reconstruction characters, coupled with segregant- and facet-dependent sophisticated compositional profiles, is prevailing in the transition metal–doped WC-Co interfaces to enable transitions in bonding characters from covalent to metallic over three atomic layers. DFT calculations advance the understanding of how the mixed bonds in ceramics are transited to metallic bonds across the WC-Co interface. The directional covalent bonding promotes the formation of the reconstructed interfacial trilayers coherent with the underneath WC grains, while the increasing fraction of segregated metal solutes toward the metallic bulk Co phase creates a rather gradual transition in electronic structures. Some unique features of the Ti-, V-, and Cr-doped WC-Co interfaces revealed in this study may also exist in other metal-ceramic interfaces. This study exemplifies a case of sophisticated interfaces between metals and (mostly) covalent ceramics with unprecedented details of the interfacial structure, composition, and bonding character revealed simultaneously, all at atomic levels.

MATERIALS AND METHODS
Sample preparation
The WC-Co samples were prepared by Xiamen Tungsten Industry Co. Ltd. using the typical sintering and processing procedures adopted for the industrial production. Tungsten carbide (WC) hard metals with ~10.0 weight % of Co were prepared by a standard powder metallurgical process with liquid-phase sintering. The commercial WC, transition metal carbides, and Co powders with Fisher particle sizes of 4.0, 1.5, and 0.8 μm, respectively, were produced by Xiamen Tungsten Industry Co. Ltd. Next, these powders were mixed and milled as starting materials via a vacuum drying process to produce granulated powders. The doping concentration for each transition-metal element (Ti, V, or Cr) is set to 0.38 atomic % on the metal basis for all specimens to examine the segregation behaviors at the WC-Co interfaces. Subsequently, they were pressed in a mold with pressure of 150 MPa, followed by a dewaxing process. Last, all specimens were sintered in vacuum following the same produce described below. The temperature was first elevated to 1450°C with a heating rate of 3°C/min above 1200°C. Then, all specimens were sintered isothermally at 1450°C for 1 hour. Fully dense samples were cooled down to room temperature with a cooling rate of 5° to 20°C/min.

TEM and STEM characterization
We used FIB to prepare thin TEM lamellae for the aberration-corrected TEM observation. The lamellae thickness was controlled in a range of 50 to 60 nm to ensure comparable STEM imaging and spectrum analysis. All the HAADF, LAADF, iDPC images, atomic-resolution EDS mapping, and EELS spectra were recorded on a Thermo Fisher Scientific TEM (Themis Z, 300 kV). The collection angle of iDPC, LAADF, and HAADF imaging was 12 to 45, 48 to 200, and 61 to 200 mrad, respectively.

Specifically, EELS spectra were recorded under the STEM mode. A scanning box was placed on specific layer, e.g., a L0 layer, with which the scanning electron beam was confined. An EELS collection angle of 100 mrad was used. The core-loss spectrum was integrated in the box, followed with deconvolution using the low-loss spectrum recorded from the same box to remove the plural scattering effect. The deconvoluted core-loss spectrum thus represented the bonding status of this specific layer. For the representation or comparison of EELS spectra from different layers, the spectra were normalized by setting the pre-edge background to 0 and the L3 peak to 255, using a self-made code. The white line ratios (L3/L2) were derived following Jason's algorithm (*35*) and implemented by a self-made code.

EBSD analysis
EBSD was used to determine the interfacial orientation relations. The samples were prepared by mechanical grinding and subsequent mechanical polishing. The EBSD measurement was carried out using a Zeiss SEM (Gemini 500) equipped with an Oxford Aztec EBSD system working at 20 kV. The working distance and the scanning step size were 10 mm and 0.25 μm, respectively. The lines in

these maps indicate phase boundaries or high-angle grain boundaries (GBs) with a misorientation larger than 15°.

First principles calculations

The Vienna Ab initio Simulations Package (VASP) code was used to perform first principles DFT calculations (45, 46). The Kohn-Sham equations were solved by using the projected-augmented wave method (47, 48). The nonlocal optB86b-vdW functional was selected for structural optimization of WC interfacial structures based on prior work (17). Because of the large crystal structure, the Brillouin zone integrations were sampled on a Γ-centered $1 \times 1 \times 1$ grid. The kinetic energy cutoff for plane waves was set to 400 eV, the convergence criterion for electronic self-consistency was set to 5×10^{-4} eV, and the "medium" precision setting was used. The lattice parameters of WC interface structure were kept unchanged, and only atomic positions were subjected to fully relax until the force components on atoms were smaller than 0.02 eV/Å. The vacuum region is set to ~12 Å to isolate the interactions between WC and Co slabs. The generalized gradient approximation + U method with $U = 3.0$ and $J = 1.0$ eV were considered for Ti d-electrons (17), $U = 3.25$ and $J = 1.0$ eV were considered for V d-electrons (40), and $U = 3.7$ and $J = 1.0$ eV were considered for Cr d-electrons (40). The fully optimized structures were used to perform static calculations for electronic structure under a Γ-centered $2 \times 2 \times 1$ grid. The spin-polarized effect was not considered because of its weak effect.

SUPPLEMENTARY MATERIALS

Supplementary material for this article is available at http://advances.sciencemag.org/cgi/content/full/7/11/eabf6667/DC1

REFERENCES AND NOTES

1. S. B. Sinnott, E. C. Dickey, Ceramic/metal interface structures and their relationship to atomic- and meso-scale properties. *Mat. Sci. Eng. R* **43**, 1–59 (2003).
2. M. W. Finnis, The theory of metal-ceramic interfaces. *J. Phys. Condens. Matter* **8**, 5811–5836 (1996).
3. A. Bogicevic, D. R. Jennison, Variations in the nature of metal adsorption on ultrathin Al_2O_3 films. *Phys. Rev. Lett.* **82**, 4050–4053 (1999).
4. G. Renaud, Oxide surfaces and metal/oxide interfaces studied by grazing incidence x-ray scattering. *Surf. Sci. Rep.* **32**, 5–90 (1998).
5. K. Matsunaga, T. Sasaki, N. Shibata, T. Mizoguchi, T. Yamamoto, Y. Ikuhara, Bonding nature of metal/oxide incoherent interfaces by first-principles calculations. *Phys. Rev. B* **74**, 125423 (2006).
6. P. Y. Hou, J. Stringer, Oxide scale adhesion and impurity segregation at the scale/metal interface. *Oxid. Met.* **38**, 323–345 (1992).
7. D. P. Cann, C. A. Randall, Segregation in bimetallic alloys and its influence on wetting on a positive temperature coefficient resistor $BaTiO_3$ ceramic. *J. Appl. Phys.* **90**, 5698–5702 (2001).
8. P. R. Cantwell, M. Tang, S. J. Dillon, J. Luo, G. S. Rohrer, M. P. Harmer, Grain boundary complexions. *Acta Mater.* **62**, 1–48 (2014).
9. M. Tang, W. C. Carter, R. M. Cannon, Diffuse interface model for structural transitions of grain boundaries. *Phys. Rev. B* **73**, 024102 (2006).
10. W. D. Kaplan, D. Chatain, P. Wynblatt, W. C. Carter, A review of wetting versus adsorption, complexions, and related phenomena: The rosetta stone of wetting. *J. Mater. Sci.* **48**, 5681–5717 (2013).
11. P. R. Cantwell, T. Frolov, T. J. Rupert, A. R. Krause, C. J. Marvel, G. S. Rohrer, J. M. Rickman, M. P. Harmer, Grain boundary complexion transitions. *Annu. Rev. Mater. Sci.* **50**, 465–492 (2020).
12. M. Baram, D. Chatain, W. D. Kaplan, Nanometer-thick equilibrium films: The interface between thermodynmaics and atomistics. *Science* **332**, 206–209 (2011).
13. Z. Yu, Q. Wu, J. M. Rickman, H. M. Chan, M. P. Harmer, Atomic-resolution observation of Hf-doped alumina grain boundaries. *Scripta Mater.* **68**, 703–706 (2013).
14. J. F. Nie, Y. M. Zhu, J. Z. Liu, X. Y. Fang, Periodic segregation of solute atoms in fully coherent twin boundaries. *Science* **340**, 957–960 (2013).
15. Z. Yu, P. R. Cantwell, Q. Gao, D. Yin, Y. Zhang, N. Zhou, G. S. Rohrer, M. Widom, J. Luo, M. P. Harmer, Segregation-induced ordered superstructures at general grain boundaries in a nickel-bismuth alloy. *Science* **358**, 97–101 (2017).
16. N. Zhou, Z. Yu, Y. Zhang, M. P. Harmer, J. Luo, Calculation and validation of a grain boundary complexion diagram for Bi-doped Ni. *Scr. Mater.* **130**, 165–169 (2017).
17. Z. Luo, C. Hu, L. Xie, H. Nie, C. Xiang, X. Gu, J. He, W. Zhang, Z. Yu, J. Luo, A highly asymmetric interfacial superstructure in WC: Expanding the classic grain boundary segregation and new complexion theories. *Mater. Horiz.* **7**, 173–180 (2020).
18. J. Luo, H. Cheng, K. M. Asl, C. J. Kiely, M. P. Harmer, The role of a bilayer interfacial phase on liquid metal embrittlement. *Science* **333**, 1730–1733 (2011).
19. G. Duscher, M. F. Chisholm, U. Alber, M. Ruhle, Bismuth-induced embrittlement of copper grain boundaries. *Nat. Mater.* **3**, 621–626 (2004).
20. J. A. S. Ikeda, Y.-M. Chiang, Space charge segregation at grain boundaries in titanium dioxide: I, Relationship between lattice defect chemistry and space charge potential. *J. Am. Ceram. Soc.* **76**, 2437–2446 (1993).
21. J. A. S. Ikeda, Y.-M. Chiang, A. J. Garratt-Reed, J. B. Vandersande, Space charge segregation at grain boundaries in titanium dioxide: II, Model experiments. *J. Am. Ceram. Soc.* **76**, 2447–2459 (1993).
22. H.-I. Yoon, D.-K. Lee, H. B. Bae, G.-Y. Jo, H.-S. Chung, J.-G. Kim, S.-J. L. Kang, S.-Y. Chung, Probing dopant segregation in distinct cation sites at perovskite oxide polycrystal interfaces. *Nat. Commun.* **8**, 1417 (2017).
23. T. Yamamoto, Y. Ikuhara, T. Watanabe, T. Sakuma, Y. Taniuchi, K. Okada, T. Tanase, High resolution microscopy study in Cr_3C_2-doped WC-Co. *J. Mater. Sci.* **36**, 3885–3890 (2001).
24. A. Delanoë, M. Bacia, E. Pauty, S. Lay, C. H. Allibert, Cr-rich layer at the WC/Co interface in Cr-doped WC–Co cermets: Segregation or metastable carbide? *J. Cryst. Growth* **270**, 219–227 (2004).
25. A. Meingast, E. Coronel, A. Blomqvist, S. Norgren, G. Wahnström, M. Lattemann, High resolution STEM investigation of interface layers in cemented carbides. *Int. J. Refract. Met. Hard Mater.* **72**, 135–140 (2018).
26. S. Lay, S. Hamar-Thibault, A. Lackner, Location of VC in VC, Cr_3C_2 codoped WC-Co cermets by HREM and EELS. *Int. J. Refract. Met. Hard Mater.* **20**, 61–69 (2002).
27. S. Lay, J. Thibault, S. Hamar-Thibault, Structure and role of the interfacial layers in VC-rich WC-Co cermets. *Philos. Mag.* **83**, 1175–1190 (2003).
28. S. Lay, S. Hamar-Thibault, M. Loubradou, Accommodation of the lattice mismatch at the VC_x-WC interface. *Interface Sci.* **12**, 187–195 (2004).
29. I. Sugiyama, Y. Mizumukai, T. Taniuchi, K. Okada, F. Shirase, T. Tanase, Y. Ikuhara, T. Yamamoto, Three-dimensional morphology of $(W,V)C_x$ in VC-doped WC–Co hard metals. *Scripta Mater.* **69**, 473–476 (2013).
30. L. Lin, Z. Lin, J. Zhang, X. Cai, W. Lin, Z. Yu, X. Wang, Molecular-level insights on the reactive facet of carbon nitride single crystals photocatalysing overall water splitting. *Nat. Catal.* **3**, 649–655 (2020).
31. X. Liu, X. Song, H. Wang, X. Liu, F. Tang, H. Lu, Complexions in WC-Co cemented carbides. *Acta Mater.* **149**, 164–178 (2018).
32. S. A. E. Johansson, G. Wahnström, A computational study of thin cubic carbide films in WC/Co interfaces. *Acta Mater.* **59**, 171–181 (2011).
33. S. A. E. Johansson, G. Wahnström, Theory of ultrathin films at metal–ceramic interfaces. *Phil. Mag. Lett.* **90**, 599–609 (2010).
34. T. Yamamoto, Y. Ikuhara, T. Sakuma, High resolution transmission electron microscopy study in VC-doped WC-Co compound. *Sci. Technol. Adv. Mater.* **1**, 97–104 (2000).
35. J. Graetz, C. C. Ahn, H. Ouyang, P. Rez, B. Fultz, White lines and d-band occupancy for the 3d transition-metal oxides and lithium transition-metal oxides. *Phys. Rev. B* **69**, 235103 (2004).
36. D. H. Pearson, C. C. Ahn, B. Fultz, White lines and d-electron occupancies for the 3d and 4d transition metals. *Phys. Rev., B Condens. Matter* **47**, 8471–8478 (1993).
37. C. Hu, J. Huang, B. G. Sumpter, E. Meletis, T. Dumitrica, Ab initio predictions of hexagonal Zr(B,C,N) polymorphs for coherent interface design. *J. Phys. Chem. C* **121**, 26007–26018 (2017).
38. Y. Li, Y. Gao, B. Xiao, T. Min, Y. Yang, S. Ma, D. Yi, The electronic, mechanical properties and theoretical hardness of chromium carbides by first-principles calculations. *J. Alloy Compd.* **509**, 5242–5249 (2011).
39. Y. Li, B. Hu, B. Liu, A. Nie, Q. Gu, J. Wang, Q. Li, Insight into Si poisoning on grain refinement of Al-Si/Al-5Ti-B system. *Acta Mater.* **187**, 51–65 (2020).
40. A. Jain, S. P. Ong, G. Hautier, W. Chen, W. D. Richards, S. Dacek, S. Cholia, D. Gunter, D. Skinner, G. Ceder, K. A. Persson, Commentary: The materials project: A materials genome approach to accelerating materials innovation. *APL Mater.* **1**, 011002 (2013).
41. W. Guo, K. Li, Y. du, Z. Zhang, T. Xu, C. Yin, Z. Zhang, P. Zhou, X. Liu, B. Huang, Microstructure and composition of segregation layers at WC/Co interfaces in ultrafine-grained cemented carbides co-doped with Cr and V. *Int. J. Refract. Met. Hard Mater.* **58**, 68–73 (2016).
42. J. Weidow, H.-O. Andrén, Grain and phase boundary segregation in WC–Co with TiC, ZrC, NbC or TaC additions. *Int. J. Refract. Met. Hard Mater.* **29**, 38–43 (2011).
43. M. Kawakami, O. Terada, K. Hayashi, Effect of sintering cooling rate on V segregation amount at WC/Co interface in VC-doped WC-Co fine grained hardmetal. *J. Jpn. Soc. Powder Powder Metall.* **51**, 576–585 (2004).

44. K. Okada, A. Osada, Microstructural study on the grain growth inhibition of VC-doped WC-Co cemented carbides. *Int. J. Refract. Met. Hard Mater.* **62**, 149–154 (2017).

45. G. Kresse, J. Hafner, Ab initio molecular dynamics for liquid metals. *Phys. Rev. B* **47**, 558–561 (1993).

46. G. Kresse, J. Furthmüller, Efficient iterative schemes for ab initio total-energy calculations using a plane-wave basis set. *Phys. Rev. B* **54**, 11169–11186 (1996).

47. P. E. Blöchl, Projector augmented-wave method. *Phys. Rev. B* **50**, 17953–17979 (1994).

48. G. Kresse, D. Joubert, From ultrasoft pseudopotentials to the projector augmented-wave method. *Phys. Rev. B* **59**, 1758 (1999).